

Low-energy termination of spiral turbulence in heterogeneous myocardium using circularly polarized electric fields

Yu-Jie Lv(吕玉杰), Xia Feng(冯霞), Wan-Jie Mei(梅万杰), Kai-Wen Sun(孙凯文), Chun Zhang(张春), and Xiang Gao(高翔)

Citation: Chin. Phys. B, 2026, 35 (**3**): 038201. DOI: 10.1088/1674-1056/ae24ee
http://cpb.iphy.ac.cn; http://iopscience.iop.org/cpb

What follows is a list of articles you may be interested in

Turing instability-induced oscillations in coupled reaction-diffusion systems

Nan Wang(王楠), Yuan Tong(仝源), Fucheng Liu(刘富成), Xiaoxuan Li(李晓璇), Yafeng He(贺亚峰), and Weili Fan(范伟丽)
Chin. Phys. B, 2025, 34 (**3**): 038201. DOI: 10.1088/1674-1056/ada42b

Unpinning the spiral waves by using parameter waves

Lu Peng(彭璐) and Jun Tang(唐军)
Chin. Phys. B, 2021, 30 (**5**): 058202. DOI: 10.1088/1674-1056/abd46e

Exploring the role of inhibitory coupling in duplex networks

Cui-Yun Yang(杨翠云), Guo-Ning Tang(唐国宁), Hai-Ying Liu(刘海英)
Chin. Phys. B, 2017, 26 (**8**): 088201. DOI: 10.1088/1674-1056/26/8/088201

Numerical simulation and analysis of complex patterns in a two-layer coupled reaction diffusion system

Li Xin-Zheng (李新政), Bai Zhan-Guo (白占国), Li Yan (李燕), He Ya-Feng (贺亚峰), Zhao Kun (赵昆)
Chin. Phys. B, 2015, 24 (**4**): 048201. DOI: 10.1088/1674-1056/24/4/048201

Low-energy termination of spiral turbulence in heterogeneous myocardium using circularly polarized electric fields

Yu-Jie Lv(吕玉杰)[1], Xia Feng(冯霞)[1,†], Wan-Jie Mei(梅万杰)[1], Kai-Wen Sun(孙凯文)[1], Chun Zhang(张春)[1], and Xiang Gao(高翔)[2,‡]

[1] *Faculty of Science, Xi'an Shiyou University, Xi'an* 710065, *China*
[2] *School of Physics and Information Technology, Shaanxi Normal University, Xi'an* 710062, *China*

(Received 14 September 2025; revised manuscript received 8 November 2025; accepted manuscript online 27 November 2025)

Circularly polarized electric fields (CPEF) represent a highly promising low-energy defibrillation approach, demonstrating exceptional efficacy in terminating life-threatening arrhythmias such as ventricular fibrillation while effectively mitigating the myocardial injury risks associated with conventional high-voltage defibrillation. This study provides an in-depth revelation of the mechanism by which CPEF induces excitation waves around naturally occurring heterogeneous defects within heart tissue, thereby suppressing spiral turbulence. Through numerical simulations based on the LR1 model and phase field method, we confirm that CPEF, due to its dynamic rotational properties, induces virtual electrode effects around various defects. In conditions of low strength, CPEF adaptively excites these defects, thereby achieving synchronized myocardial activation for defibrillation. In comparison with uniform electric fields (UEF), CPEF is more effective in suppressing spiral turbulence by inducing periodic excitation waves around defects with irregular geometries. These findings elucidate the biophysical principles underlying CPEF's low-energy defibrillation capability, offering robust theoretical support for developing non-invasive antiarrhythmic therapies.

Keywords: spiral, pattern formation, excitable system, virtual electrode

PACS: 82.40.Ck, 87.18.Hf, 87.19.lp

DOI: 10.1088/1674-1056/ae24ee **CSTR:** 32038.14.CPB.ae24ee

1. Introduction

Arrhythmia, a cardiovascular disease characterized by abnormal electrical activity in the heart leading to rhythm disorders, poses a serious threat to human life and health.[1] Among the various forms of heart arrhythmia, ventricular fibrillation is the most critical. The condition is characterized by accelerated and uncoordinated electrical activity in the ventricular muscle, leading to the deterioration of effective cardiac contraction and ejection function. This, in turn, results in acute ischemia of vital organs, such as the heart and brain.[2] Without prompt intervention, patients can succumb to circulatory failure within minutes.[3,4] Clinically, traditional defibrillators employ high-voltage direct current shocks to forcibly reset the heart's electrical activity. While high-energy shocks are effective at terminating ventricular fibrillation and restoring sinus rhythm, they are often associated with significant pain, myocardial injury, and postoperative complications. This risk is particularly pronounced in patients suffering from ischemic heart disease, where such interventions may cause secondary damage. Consequently, the development of low-energy, low-trauma arrhythmia intervention strategies has become a major focus in electrophysiology and biomedical engineering research.[5]

In recent years, low-energy defibrillation technology based on the virtual electrode effect (VEE) has attracted considerable attention due to its non-invasive and cardioprotective properties. According to this theory, when an external electric field is applied to myocardial tissue, heterogeneity in dielectric properties triggers membrane potential redistribution and localized polarization. Should the field strength reach a certain threshold, these heterogeneities act as "virtual electrodes", thereby generating waves that promote synchronized myocardial activation.[6,7] In comparison with conventional high-voltage shocks, VEE based strategies have been shown to significantly reduce energy requirements and tissue damage by leveraging the inherent anatomical features of the heart. This offers a promising new paradigm for the treatment of arrhythmia.

The configuration of the external electric field is of pivotal importance in the implementation of VEE. A significant number of studies have employed uniform electric fields (UEF) for stimulation purposes.[8–14] While this approach facilitates the simplification of theoretical modelling, it frequently fails to align with the intricate spatial distribution of physiological defects observed in actual heart tissue. Conversely, the circularly polarized electric field (CPEF),[15] which can be formed by the superposition of two orthogonal alternating electric fields with a phase difference, provides spatial adaptability and overcomes the directional limitations of UEF. It has been demonstrated that CPEF is capable of effectively

†Corresponding author. E-mail: fengxia0709@126.com
‡Corresponding author. E-mail: gaoxiang.gnaixoag@gmail.com

© 2026 Chinese Physical Society and IOP Publishing Ltd. All rights, including for text and data mining, AI training, and similar technologies, are reserved.

eliminating spiral waves and turbulent states within chemical systems.[16–21] Experimental and computational studies have demonstrated that spiral waves in heart tissue (e.g., pinned spirals or spiral wave turbulence) bear a close resemblance to clinical tachyarrhythmia, including ventricular tachycardia and fibrillation.[22,23] In view of the findings outlined above, a significant number of research groups have undertaken systematic investigations into the CPEF induced VEE to address the elimination of pinned spiral waves (modelling re-entrant tachycardia) and spiral wave turbulence (representing ventricular fibrillation).[24–28]

As demonstrated in our previous research, in the case of singular circular or elliptical defects, CPEF has been shown to effectively terminate arrhythmia by inducing periodic excitation in dynamically polarized regions in the vicinity of the defects.[29,30] However, real myocardial tissue contains vascular networks with tree-like structures and naturally occurring defects that vary widely in size (from microns to millimeters), shape (from circular to elongated), and spatial distribution.[31] Existing single-defect models are inadequate for capturing the multi-scale behavior of CPEF in such complex anatomical environments.

Consequently, this study proposes the construction of a myocardial tissue model incorporating defects of diverse sizes, shapes, and irregular distributions, with the aim of better approximating real physiological conditions. The objective of this study is to elucidate the advantages and underlying biophysical mechanisms of CPEF in heterogeneous heart tissue by comparing the excitation efficiency, electrical wave propagation characteristics, and arrhythmia termination efficacy under UEF and CPEF stimulation. This work provides a theoretical foundation for the optimization of low-energy defibrillation techniques and supports the development of novel arrhythmia treatment devices based on electric field modulation.

2. Model and methods

2.1. Mono-domain reaction-diffusion equation

Our numerical simulations were based on the mono-domain reaction-diffusion equation to characterize ion channel currents across the ventricular cardiomyocyte membrane. The transmembrane potential ($V_{\rm m}$) and no-flux boundary conditions can be governed by

$$\partial V_{\rm m}/\partial t = -I_{\rm ion}(V_{\rm m}, y)/C_{\rm m} + \nabla \cdot D\nabla V_{\rm m}, \tag{1}$$

$$\boldsymbol{n} \cdot D\nabla V_{\rm m} = 0, \tag{2}$$

where $C_{\rm m}$ is the membrane capacitance, D is the diffusion coefficient, $I_{\rm ion}(V_{\rm m}, y)$ is the total current, y is gating variables characterizing the conductivity of various ion channels. n denotes the normal vector to the heterogeneity boundary. For the LR1 model,[32,33] $I_{\rm ion}(V_{\rm m}, y)$ consists of a fast sodium current $I_{\rm Na}$, a slow inward current $I_{\rm si}$, a time-dependent potassium current $I_{\rm K}$, a time-independent potassium current $I_{\rm K1}$, a plateau potassium current $I_{\rm Kp}$, and a time-independent background current $I_{\rm b}$. They are obtained as solutions to a coupled system of nonlinear ordinary differential equations. The differential equations are of the form $\mathrm{d}y/\mathrm{d}t = (y_\infty - y)/\tau_y$, where y represents the gating variable, τ_y is its time constant, and y_∞ is the steady-state value of y. The specific formulas refer to Refs. [32,33]. And the parameter values are those that have the potential to form turbulent waves.[34]

For the defects in myocardial media, they all have the no-flux boundary conditions. To simulate the no-flux boundary conditions in Cartesian coordinates, we use the phase field method.[35,36] The phase field method can simulate the no-flux boundary conditions on various complex geometric boundaries in Cartesian coordinates. It introduces a phase field ϕ into Eq. (1). First, ϕ is set to be 1 in the myocardial media, and 0 in the defect and outside the media. Then, we use the relaxation method to smooth the value of ϕ near no-flux boundaries. The smoothed value of ϕ is determined by the following formula:

$$\partial\phi/\partial t = \xi^2\nabla^2\phi - \partial G(\phi)/\partial\phi, \tag{3}$$

where ξ is a constant that controls the width of the boundary. And $G(\phi)$ is a double-well function whose standard form is

$$G(\phi) = -(2\phi-1)^2/4 + (2\phi-1)^4/8. \tag{4}$$

The function $G(\phi)$ has the form of a double-well potential with minima at $\phi = 0$ and $\phi = 1$. To make the partial differential Eq. (3) have a stable solution, we set the space and time step as $\mathrm{d}x^2 = 4\mathrm{d}t$. ξ can control the width of the falloff area around boundaries and is set to be $0.5\mathrm{d}x$ in our simulations.

The phase field method then consists of replacing the original diffusion term (e.g., in Eq. (1)) by a modified term that involves the phase field ϕ:

$$\begin{aligned}\nabla \cdot D\nabla V_{\rm m} &\rightarrow \frac{1}{\phi}\nabla\cdot(\phi D\nabla V_{\rm m}) \\ &\rightarrow \nabla\cdot(D\nabla V_{\rm m}) + \nabla(\ln\phi)\cdot(D\nabla V_{\rm m}).\end{aligned} \tag{5}$$

2.2. The external electric field

Defects in heart tissue can be regarded as virtual electrodes under the influence of an external electric field. In essence, defects of any geometric shape trigger redistribution of membrane potential when current flows through cellular tissue, inducing depolarization and hyper-polarization to form virtual electrodes. Specifically, as demonstrated in Fig. 1(a), when an external current passes through a cell containing a defect, it cannot traverse the discontinuity (defect boundary) and flows solely from inside to outside the cell, causing membrane potential to rise at that location. In the context of contemporary conservation measures, the movement of ions is such that

they return to the cell on the opposite side of the defect. This phenomenon results in a decline in membrane potential at that particular location. It can thus be concluded that the external electric field redistributes the membrane potential around the defect, as shown in Fig. 1(b). Depolarization, defined as the flow of current in an outward direction, a shift in membrane potential from negative inside to positive outside, and an increase in membrane potential, occurs on one side of the defect. Conversely, hyper-polarization, defined as a decrease in membrane potential, occurs on the other side. At this stage, the defect functions as a virtual electrode. In the event of an electric field strength that is sufficiently high, the depolarized region will be capable of exciting a wave.

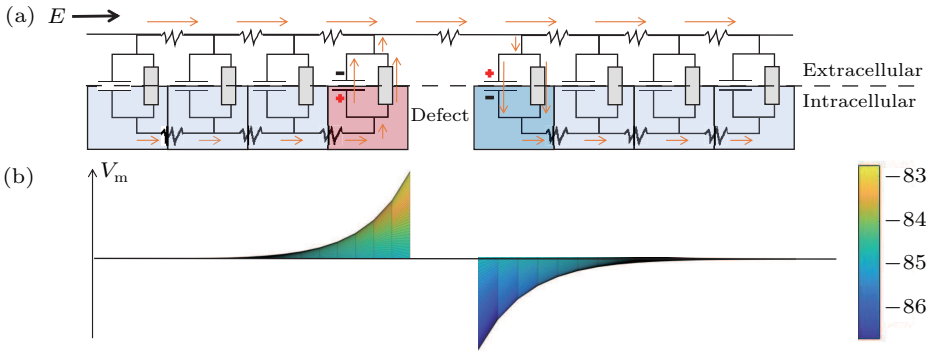


Fig. 1. Virtual electrode under the influence of an external electric field. (a) The figure refers to current flow direction inside and outside cells under an external electric field. (b) The membrane potential distribution corresponds to the applied electric field strength of 0.1 V·cm^{-1}.

The general effect of an external electric field on a defect can be mathematically represented by a Neumann boundary condition[8,37]

$$\boldsymbol{n}\cdot\nabla V_{\mathrm{m}} = \boldsymbol{n}\cdot\boldsymbol{E} \;\text{ or }\; \boldsymbol{n}\cdot(\nabla V_{\mathrm{m}} - \boldsymbol{E}) = 0, \tag{6}$$

where $\boldsymbol{E}$ is the external electric field. To apply the above Neumann boundary condition and the phase field ϕ to Eq. (1), the hypothesis under consideration is that of an isotropic organization. The diffusion coefficient is a scalar. Therefore, the following formula can be deduced:

$$\begin{aligned}\partial V_{\mathrm{m}}/\partial t \;=\; & -I_{\mathrm{ion}}(V_{\mathrm{m}}, y)/C_{\mathrm{m}} + D\nabla^2 V_{\mathrm{m}} \\ & + D\left(\nabla(\ln\phi)\cdot(\nabla V_{\mathrm{m}})\right) - \left(\nabla(\ln\phi)\cdot\boldsymbol{E}\right),\end{aligned} \tag{7}$$

when a UEF pulse was applied along the x-axis, the external electric field $\boldsymbol{E}$ in Eq. (7) took the form $\boldsymbol{E} = (E_x, 0) = (E_0, 0)$, where E_0 denotes the field strength. To emulate such a UEF under experimental conditions, a pair of positive and negative electrodes, or two pairs arranged perpendicularly around the heart, can be used to deliver direct current, thereby generating a far-field matrix pulse within the heart tissue.[10]

$$\begin{aligned}\partial V_{\mathrm{m}}/\partial t \;=\; & -I_{\mathrm{ion}}(V_{\mathrm{m}}, y)/C_{\mathrm{m}} + D\nabla^2 V_{\mathrm{m}} \\ & + D\nabla(\ln\phi)\cdot(\nabla V_{\mathrm{m}}) - DE_0\left(\partial\ln\phi/\partial x\right).\end{aligned} \tag{8}$$

For the CPEF, the same two perpendicular electrode pairs were supplied with alternating currents to produce a rotating field.[19] The CPEF was defined mathematically as

$$\boldsymbol{E}(t) = (E_x, E_y) = \left(E_0\sin(\omega t), E_0\cos(\omega t)\right), \tag{9}$$

where E_0 represents electric field strength and ω denotes the angular frequency of field rotation.[15] In such conditions, the CPEF rotates clockwise, and Eq. (7) can be expressed as follows:

$$\begin{aligned}\partial V_{\mathrm{m}}/\partial t \;=\; & -I_{\mathrm{ion}}(V_{\mathrm{m}}, y)/C_{\mathrm{m}} + D\nabla^2 V_{\mathrm{m}} + D\nabla(\ln\phi)\cdot(\nabla V_{\mathrm{m}}) \\ & - D\left(E_x\left(\partial\ln\phi/\partial x\right) + E_y\left(\partial\ln\phi/\partial y\right)\right),\end{aligned} \tag{10}$$

where the membrane capacitance C_{m} is set to be 1 μF·cm^{-2}, and the diffusion coefficient D is set to be 0.001 cm^2·ms^{-1}. In the case of two-dimensional media, the integration of Eqs. (8) and (10) is performed using the explicit Euler method. The grid utilized for this simulation is a regular lattice. The discretization of space and time is determined by referring to the study in Ref. [9], with the spatial step size set as $\Delta x = \Delta y = 0.015$ cm, and the temporal step size $\Delta t = 0.005$ ms. This parameter selection satisfies the approximate CFL stability condition, thereby ensuring the numerical scheme's stability for diffusion processes. Furthermore, following the refinement of the grid and the subsequent re-run of the simulation, no substantial alterations in the results were observed, thereby suggesting the grid independence of the outcomes under the selected grid settings. The computation of the Laplacian term $\nabla^2 V_{\mathrm{m}}$ is achieved through the implementation of a five-point-stencil finite difference method. The gradient terms $\nabla(\ln\phi)$ and ∇V_{m} are addressed by means of the central difference scheme.

3. Results

3.1. Virtual electrode-induced wave in resting myocardium

The heart is a highly heterogeneous organ, filled with defects in conduction heterogeneity. These lesions may be attributable to various etiologies, including but not limited

to blood vessels, non-myocardial area, mechanically damaged area, high-density area, cluster of severely damaged cell monolayers, and uneven area.[38] It is particularly noteworthy that blood vessels are distributed extensively throughout the heart tissue. In the domain of cardiac anatomy, it is evident that most of these structures exhibit elliptical or circular morphology. It has been demonstrated that other shapes exhibit irregularities, with their boundary curvature varying in a manner that is analogous to an ellipse.

To present the heterogeneity of the actual heart, including the presence of elliptical or circular structures such as blood vessels, a two-dimensional resting myocardial medium was constructed. This medium contained multiple heterogeneities (defects) of varying sizes and shapes with a non-uniform spatial distribution. In the numerical simulation undertaken, a medium measuring 10 cm × 10 cm was selected, with defects being introduced into the medium. The distribution, size, quantity, and orientation of these defects are randomly generated. As illustrated in Fig. 2(a), each defect (m, n, θ) is parameterized by its long semi-axis m (cm), short semi-axis n (cm), and an orientation angle θ representing the inclination relative to the x-axis.

To enhance the randomness and complexity of the simulation, the number of defects is determined by generating a random integer between 1 and 10 using a uniform pseudo-random number generator. Subsequently, the centre coordinates of each defect are randomly generated using a random scalar obtained from the same uniform pseudo-random number generator. In the subsequent stage of the process, the dimensions of each defect are defined as elliptical. The long semi-axis (m) and short semi-axis (n) of each defect are randomly generated within the range of 0.06 cm to 0.5 cm. Finally, the orientation angle (θ) of each defect is randomly generated as a random integer within the range of 0 to 2π using the uniform pseudo-random number generator. This random sampling approach ensures that the defect combination in each simulation is unique, thereby more closely approximating the complexity and unpredictability of heterogeneous structures in actual hearts.

When calculating the coordinates of defect boundary locations, the focal length c is determined based on the elliptical geometry property using the focal length formula $c^2 = m^2 - n^2$. Combining this with the center coordinates and orientation angle, the coordinates of the two foci (x_1, y_1) and (x_2, y_2) of the ellipse are computed. The calculation formula is as follows:

$$\begin{cases} x_1 = x_0 + c\cos\theta, \\ y_1 = y_0 + c\sin\theta, \end{cases} \quad \begin{cases} x_2 = x_0 - c\cos\theta, \\ y_2 = y_0 - c\sin\theta. \end{cases} \tag{11}$$

The mathematical definition of an elliptical defect can be rigorously integrated into the following elliptic equation:

$$\left((x-x_1)^2 + (y-y_1)^2\right)^{1/2} + \left((x-x_2)^2 + (y-y_2)^2\right)^{1/2} \leq 2m. \tag{12}$$

In the ensuing study, a medium containing ten defects with diverse geometries (illustrated in Fig. 2(b)) was selected for detailed elucidation. The specific dimensions and shapes of these defects are summarized in Table 1. The sizes of the defects were designed to mimic natural vascular structures, incorporating both elliptical and circular forms, and were randomly assigned to include a mix of large and small heterogeneities. Their phases were systematically varied to ensure representative coverage of different orientations. Spatial locations were randomized, resulting in a non-homogeneous distribution with regions of varying defect density.

Table 1. The shapes and sizes of ten random defects.

Defects	Long semi-axis m (cm)	Short semi-axis n (cm)	Orientation angle θ (rad)
1	0.18	0.18	0
2	0.28	0.07	0
3	0.24	0.07	$\pi/2$
4	0.16	0.06	$5\pi/12$
5	0.20	0.10	$10\pi/12$
6	0.26	0.08	$5\pi/12$
7	0.22	0.08	$11\pi/12$
8	0.14	0.06	$7\pi/12$
9	0.24	0.24	0
10	0.18	0.09	$3\pi/12$

As shown in Fig. 2(c), a continuous clockwise rotating CPEF of low voltage was applied to the resting tissue. The electric field strength was set to 0.6 V·cm^{-1}, with a fixed angular frequency 0.14 rad·ms^{-1} (this angular frequency is further employed in the following). The initial orientation of the CPEF was aligned with the y-axis, with clockwise rotation. Under the influence of the CPEF, each defect acted as a virtual electrode, leading to wave emission around its periphery. Specifically, the electric field induced a redistribution of membrane potential around each heterogeneity, forming localized polarized and depolarized regions. After approximately $t = 6$ ms of continuous field application, wave emergence was observed around the defects. By $t = 17$ ms, all defects exhibited wave initiation. Within one full cycle of electric field application, organized circular waves developed around every defect and began propagating outward into the medium.

We study the influence of the strength E_0 and angular frequency of the CPEF ω_{CPEF} on excitation waves. When $E_0 < 0.5$ V·cm^{-1}, the transmembrane potential around the defects cannot reach the excitation threshold. The excitation wave cannot be stimulated around the defects to form a wave train. Consequently, when the E_0 increases to a sufficient level, it becomes possible to sustainably excite waves. It is noteworthy that the frequency of the generated excited wave train ω_{Wave} displays stability and remains constant in the presence

of higher electric field strengths, as demonstrated in Fig. 2(e). However, it has been demonstrated that variations in the ω_{CPEF} directly influence the ω_{Wave}. As illustrated in Fig. 2(f), the ω_{Wave} displays a 2:1, 3:1, 4:1 locking relationship[4,39,40] as ω_{CPEF} increases. It is also noteworthy that in instances where the ω_{CPEF} is excessively low or during transitional phase ratios, turbulent phenomena may emerge. These specific cases are not documented in this study.

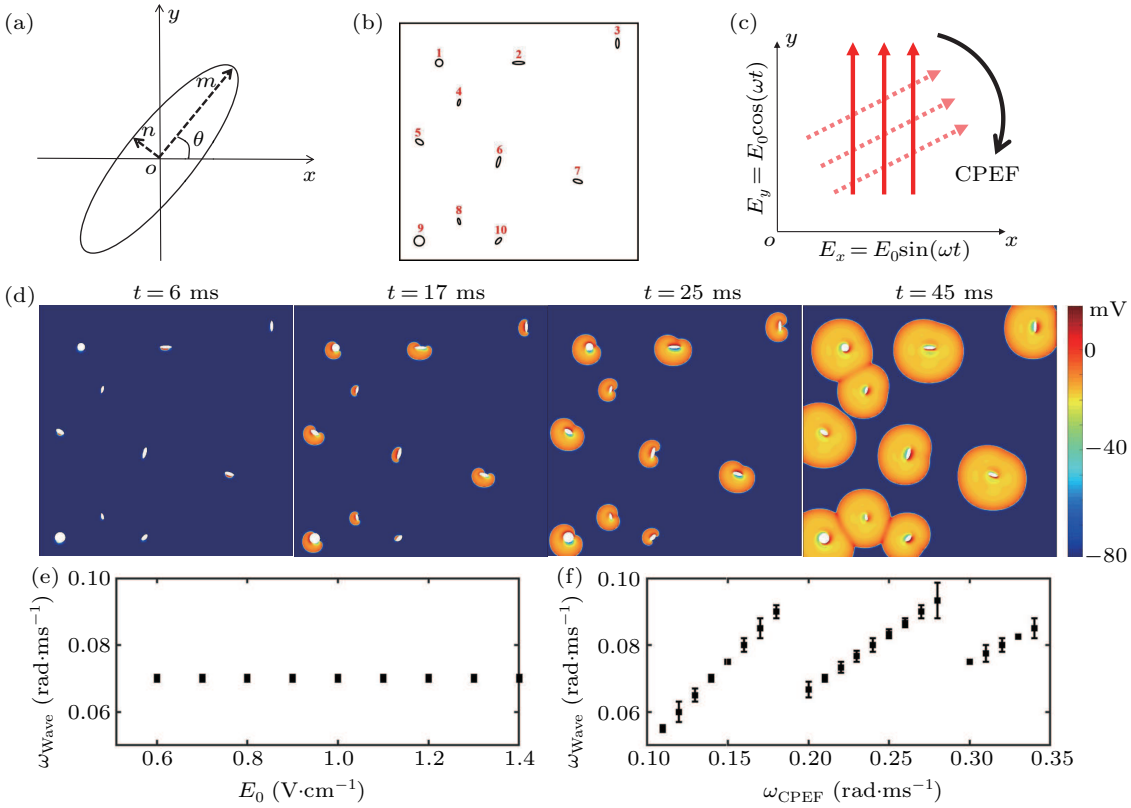


Fig. 2. Waves induced by CPEF. (a) Defects parameter setting. (b) Distribution diagram of random defects in medium. (c) Clockwise rotating CPEF. (d) Wave emission under the CPEF. The electric strength is 0.6 V·cm^{-1}. The angular frequency is 0.14 rad·ms^{-1}. Excitation wave angular frequency ω_{Wave} versus response electric field strength E_0 (e) and angular frequency ω_{CPEF} (f).

In a similar manner, Fig. 3 demonstrates the application of a series of low-voltage UEF pulses to the same myocardial medium, with an electric field strength that is identical to that employed in the CPEF case. The pulse duration was fixed to 10 ms and the pulse period to 90 ms (these parameters remained unchanged in all subsequent UEF simulations). It is evident that, due to the directional nature of the UEF, its effect on the VEE around each defect is highly orientation-dependent. In order to comprehensively evaluate this directional influence, the UEF was applied separately along the x-axis and y-axis and the outcomes were compared.

As demonstrated in Fig. 3(a), upon the application of the UEF along the y-axis, wave initiation was observed in the vicinity of specific defects, commencing at $t = 6$ ms. By 17 ms, a greater number of defects exhibited wave emission; however, four defects still failed to elicit any excitation and remained unexcited until at least 45 ms. Furthermore, as illustrated in Fig. 3(b), when the electric field was oriented along the x-axis, three defects did not generate any waves. The results indicate that, irrespective of the direction of application, the UEF is unable to induce wave emission from all defects. This finding highlights the limitation imposed by its directional dependence on effectively stimulating VEE across a heterogeneous tissue region.

In order to provide further elucidation on the wave generation behavior in the context of UEF stimulation, a classification and analysis of the defects was conducted on the basis of their capacity to induce wave emission. As demonstrated in Fig. 2, the defects can be categorized into three distinct types.

Type I: defects 1, 9, and 10, which generated waves under both UEF_y and UEF_x orientations.

Type II: defects 2, 5, and 7, which produced waves only under UEF_y.

Type III: defects 3, 4, 6, and 8, which responded exclusively to UEF_x.

In order to investigate the underlying electrophysiological mechanisms, one representative defect from each category (defect 1, defect 2, and defect 3) was selected and the temporal evolution of the membrane potential around each defect under electric field stimulation was monitored. The initiation of waves is contingent on the membrane potential's ability to surpass a designated excitation threshold. Consequently, our primary focus is directed towards the maximum potential value that undergoes temporal fluctuations. As demonstrated

in Fig. 4, the membrane potential surrounding each defect was recorded over a 200 ms period under the respective electric field conditions. It is important to note that all simulations were performed under a weak electric field with a strength of 0.1 V·cm^{-1}.

As demonstrated in Fig. 4(a), under conditions of CPEF stimulation, the maximum membrane potentials of defect 1, defect 2, and defect 3 were recorded at −78.96 mV, −78 mV, and −78.04 mV, respectively. As these values increase with the increase of electric field strength, when the electric field strength is high enough, it will exceed the excitation threshold and successfully trigger waves around each defect.

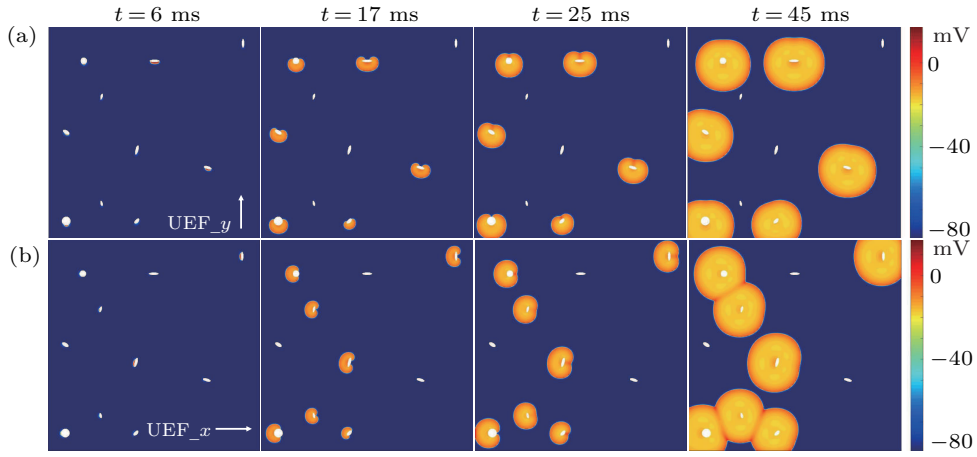


Fig. 3. Wave emission under the UEF. (a) The electric field is vertical. (b) The electric field is horizontal. The electric strength is 0.6 V·cm^{-1}. Pulses of electric field were delivered with duration 10 ms and period 90 ms.

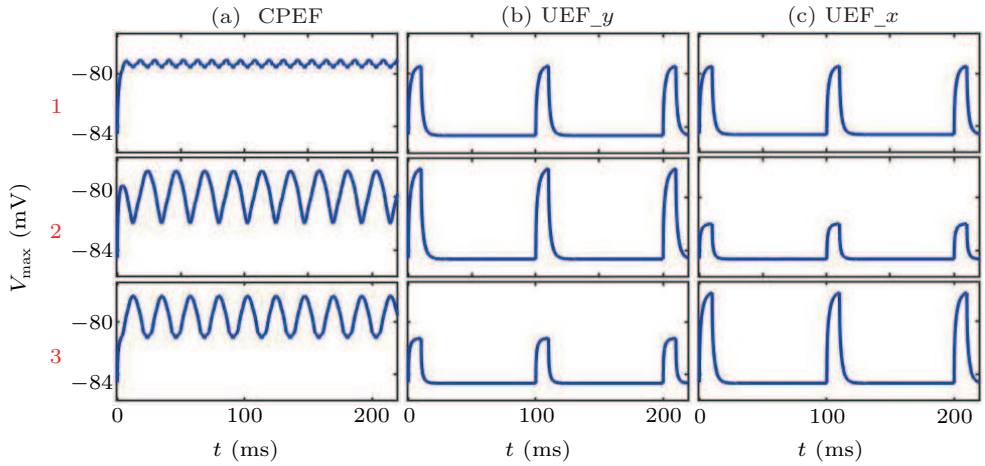


Fig. 4. The maximum membrane potentials V_{max} over time t. The CPEF (a) and UEF (b)–(c) are applied at the same weak electric strength of 0.1 V·cm^{-1}.

Conversely, when UEF is applied along the y-axis (see Fig. 4(b)), the membrane potential surrounding defect 3 attains a maximum value of −81.24 mV, exhibiting minimal sensitivity to the external electric field. Concurrently, defects 1 and 2 manifested maximum membrane potentials of −79.44 mV and −77.78 mV, respectively. In a similar manner, upon the application of the UEF along the x-axis (see Fig. 4(c)), the membrane potential surrounding defect 2 attained a maximum of −81.98 mV, which persisted at a low level. Conversely, defects 1 and 3 attained values of −79.44 mV and −77.86 mV, respectively. These observations are consistent with the wave generation patterns depicted in Figs. 3(a) and 3(b), thereby providing a biophysical rationale for the differential responses of the defects to UEF stimulation.

As demonstrated above, defect 1 is characterized by a circular nature, while defects 2 and 3 exhibit an elliptical form. As shown in Fig. 4, the maximum membrane potential induced around circular and elliptical defects under external electric field stimulation exhibits notable differences. In order to investigate this phenomenon, defects 1 and 2 were selected for further analysis. The temporal variation of membrane potential around each defect is examined by monitoring three specific locations on their boundaries. As shown in Fig. 5(a), for circular defect 1, the curvature remains constant at all three locations. Conversely, for the elliptical defect 2, the curvature is maximum at locations a and c, and minimal at location b.

Firstly, the application of a CPEF with an electric field strength of 0.1 V·cm^{-1} and an angular frequency of 0.14 rad·ms^{-1} is considered, corresponding to a period of approximately 44.86 ms. As demonstrated in Fig. 5(b), the tem-

poral variations in membrane potential at locations 1a, 1b, and 1c of the circular defect (defect 1) under CPEF exhibit similar waveforms, differing primarily in phase due to the rotation of the electric field. This behavior is the result of the continuous redistribution of membrane potential into depolarized and hyper-polarized regions, which shifts position in synchrony with the rotating CPEF.

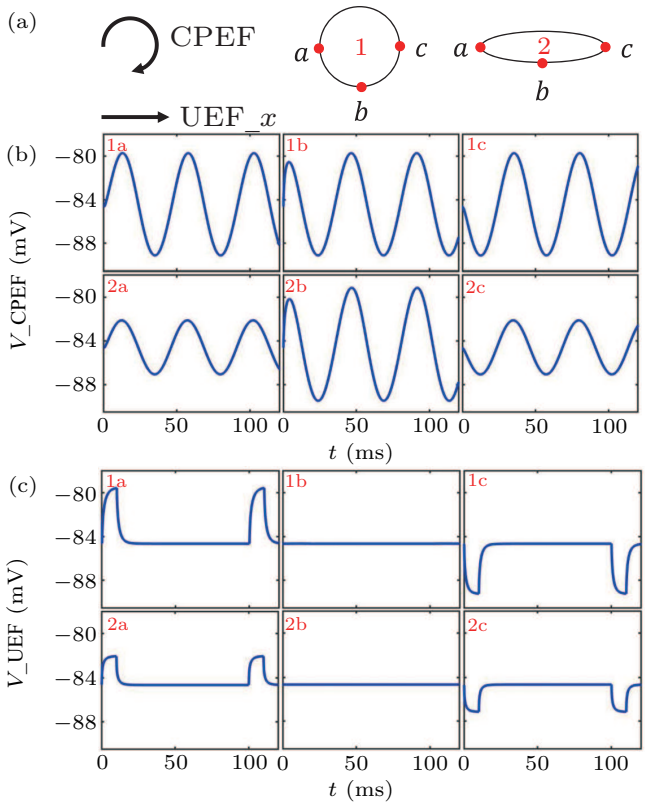


Fig. 5. The membrane potential around defects 1 and 2. (a) Location diagram of a, b and c on defects 1 and 2. CPEF is clockwise rotating and the initial direction is along the y axis. UEF is along the x axis. (b) and (c) The changes of the membrane potential over time under CPEF and UEF. The electric field strengths are all 0.1 V·cm^{-1}.

Specifically, as outlined in Table 2, the times at which the membrane potential reaches its maximum at each location were recorded. Initially aligned with the y-axis, the CPEF induces periodic changes in polarization as it undergoes rotation. For the circular defect 1, at $t = 3.85$ ms, location 1b becomes depolarized and reaches a peak potential of -80.55 mV. At $t = 46.5$ ms, another peak of -79.75 mV occurs. It is evident that at $t = 13.3$ ms, location 1a enters a depolarized state, peaking at -79.75 mV. This is followed by another peak of -79.75 mV at $t = 57.7$ ms. In a similar manner, location 1c attains maximum values of -79.75 mV at $t = 35.4$ ms and $t = 80.2$ ms. As demonstrated in Fig. 5(b), these peak variations exhibit a periodic pattern. The time intervals between consecutive peaks at locations 1a, 1b, and 1c' are 42.65, 44.4, and 44.8 ms, respectively, and align closely with the rotation period of the CPEF. The sequential activation intervals between successive peak events are 9.45 ms, 21.1 ms, 11.2 ms, and 22.5 ms. Subsequent to the application of the CPEF, the initial depolarized region is identified as location 1b. After approximately one-quarter of a rotation cycle, depolarization shifts to location 1a, and following an additional half cycle, to location 1c. The uniform curvature of the circular defect enables the membrane potential to attain comparable maximum values at each location over time. It should be noted that the initial peak following electric field application may deviate slightly due to the influence of the medium's initial state.

Table 2. Maximum membrane potential and time at each defect location via CPEF.

	Location	Maximum membrane potential (mV)	Time (ms)
Circular defect 1	a	−79.75	13.30
		−79.75	57.70
	b	−80.55	3.85
		−79.75	46.50
	c	−79.75	35.40
		−79.75	80.20
Elliptical defect 2	a	−82.13	12.20
		−82.13	57.10
	b	−80.17	4.25
		−79.15	46.85
	c	−82.13	34.65
		−82.13	79.55

In a similar manner, for the elliptical defect (defect 2), the membrane potential at location 2b peaks at -80.17 mV and -79.15 mV at 4.25 ms and 46.85 ms, respectively. At location 2a, the membrane potential reaches a maximum of -82.13 mV at 12.2 ms and 57.1 ms, while at location 2c, it peaks at -82.13 mV at 34.65 ms and 79.55 ms. The time intervals between these two consecutive peaks are 42.65 ms, 44.4 ms, and 44.8 ms, which closely match the rotational period of the CPEF. The sequential activation time intervals between successive peaks are 7.95 ms, 22.45 ms, 10.25 ms and 22.45 ms. In accordance with the behavior observed in the circular defect, location 2b initially functions as the depolarized region. Subsequent to approximately one-quarter of a cycle, the depolarization shifts to location 2a, and after an additional half cycle, to location 2c. However, as demonstrated in Fig. 5(b), the membrane potential responses at locations 2a, 2b, and 2c of the elliptical defect manifest substantial disparities beyond the phase shift induced by the CPEF rotation. These variations are attributed to disparities in local curvature. Specifically, at location 2a, where the curvature is relatively high, the peak membrane potential is comparatively low. Conversely, at location 2b, characterized by the smallest curvature, the membrane potential attains its maximum amplitude. In a similar manner, the peak value at location 2c, which is also a high-curvature region, is reduced.

In the following section, the response to the application of a UEF will be examined. The UEF has an electric field strength of 0.1 V·cm^{-1}, a pulse interval of 90 ms, and a pulse duration of 10 ms. As demonstrated in Fig. 5(c), upon the

application of the UEF along the x-axis, the membrane potential within both circular defect 1 and elliptical defect 2 is redistributed into depolarized and hyper-polarized regions, the positions of which remain constant over time. In both defects, region 1a becomes depolarized, and the membrane potential rapidly reaches its maximum. It is evident that, owing to the low curvature at 1a in the circular defect, the membrane potential attains a value of -79.68 mV. Conversely, at the same location in the elliptical defect, where the curvature is higher, the membrane potential reaches only -82.1 mV. Following an additional UEF cycle, the membrane potential once again attains its maximum value at this particular location. Concurrently, region 1c becomes hyper-polarized, and its membrane potential rapidly declines to the minimum value, undergoing a cyclical pattern with each subsequent pulse. At location 1b, which is situated precisely on the boundary between the depolarized and hyper-polarized regions, the membrane potential remains largely unchanged throughout the stimulation.

Consequently, for circular defects, waves can be elicited promptly after the application of either CPEF or UEF, provided that the radius is sufficiently large to exceed the excitation threshold and the electric field strength is adequate. In the case of elliptical defects, however, the response is found to be dependent on the electric field type. In the context of UEF, the phenomenon of depolarization frequently aligns with regions characterized by elevated curvature. This occurrence can lead to a diminution in the maximum achievable membrane potential, which may not attain the threshold necessary for the initiation of waves, even in the presence of substantial external fields. Conversely, the application of a rotating CPEF enables a continuous shift in the direction of the field, thereby allowing the polarization to align periodically with regions of reduced curvature. In such regions, the membrane potential can attain higher values, thus facilitating wave excitation provided that the field strength is sufficiently high. This differential behavior elucidates the distinct patterns of wave generation via the VEE observed in Figs. 2 and 3 under the two electric field configurations.

It has been established that under CPEF, a greater number of defects can elicit VEE, initiate circular waves, and support their outward propagation. It was demonstrated that upon the application of an external electric field with a strength of 0.6 V·cm^{-1} for a considerable duration, each defect functions as a virtual electrode. This results in the periodic generation of excitation waves along the periphery of the defect, in synchrony with the rotating field. This phenomenon is illustrated in Fig. 6(a). Conversely, the behavior exhibited under UEF is distinctly divergent. It is evident that during the process of UEF generating excitation waves, each defect will generate excitation waves and propagate outward, thereby affecting the excitation waves generated by other surrounding defects. Consequently, not all defects invariably generate excitation waves in a continuous manner. As demonstrated in Figs. 6(b) and 6(c), the excitation waves generated by each defect were observed under prolonged application of UEF. Upon the application of the UEF along the y-axis at $t = 0.325$ s, six defects (1, 2, 5, 7, 9, and 10) effectively generated excitation waves. However, in the subsequent cycle at $t = 0.435$ s, no excitation wave was produced around defect 10 (highlighted by a red dotted circle). This failure was observed to persist into the third cycle at $t = 0.530$ s. In a similar manner, when the UEF was applied along the x-axis at $t = 0.326$ s, excitation waves emerged around seven defects (1, 3, 4, 6, 8, 9, and 10). However, during the second and third cycles, defects 8 and 10 ceased to generate waves. It is evident that while UEF has the capacity to instigate the propagation of excitation waves, the number of defects capable of sustaining wave emission diminishes over time due to mutual wave interference. Numerical simulations have been conducted to investigate the efficacy of utilizing UEF applied along the y-axis or along the x-axis in terminating spiral wave turbulence. The results obtained from our simulations have confirmed that neither UEF application could effectively terminate the turbulent state.

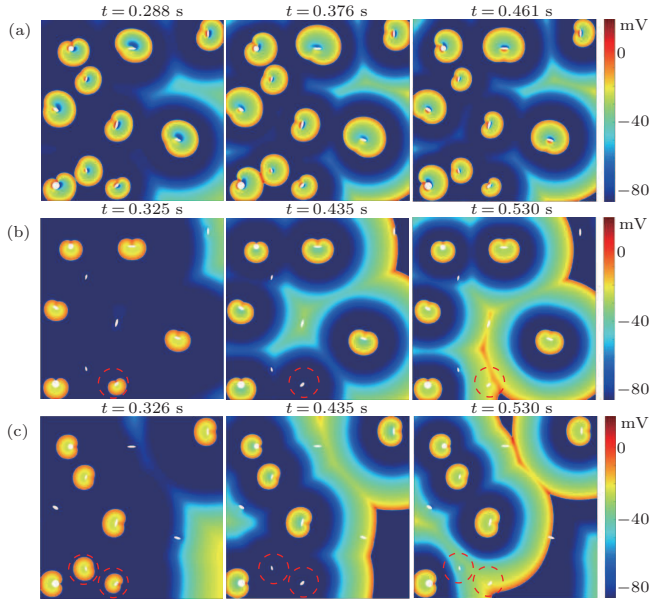


Fig. 6. Waves emission. (a) Applied CPEF with clockwise rotation along the y axis in the initial direction. The electric strength is 0.6 V·cm^{-1}. (b) and (c) The directions of UEF are vertical and horizontal, respectively. The electric strengths are all 0.6 V·cm^{-1}.

3.2. Effective termination of turbulence by dynamically adaptive CPEF

It has been demonstrated that CPEF has the capacity to promote the periodic and sustained generation of excitation waves in the vicinity of each defect. The present study investigated the phenomenon of CPEF induced VEE in the presence of spiral wave turbulence within the myocardial medium. In the absence of external intervention, the medium remains in a persistent turbulent state characterized by continuously evolving spiral waves, whose number and location are subject to

change due to mutual collisions and propagation. As demonstrated in Fig. 7(a), these free spiral waves can be observed traversing the defect.

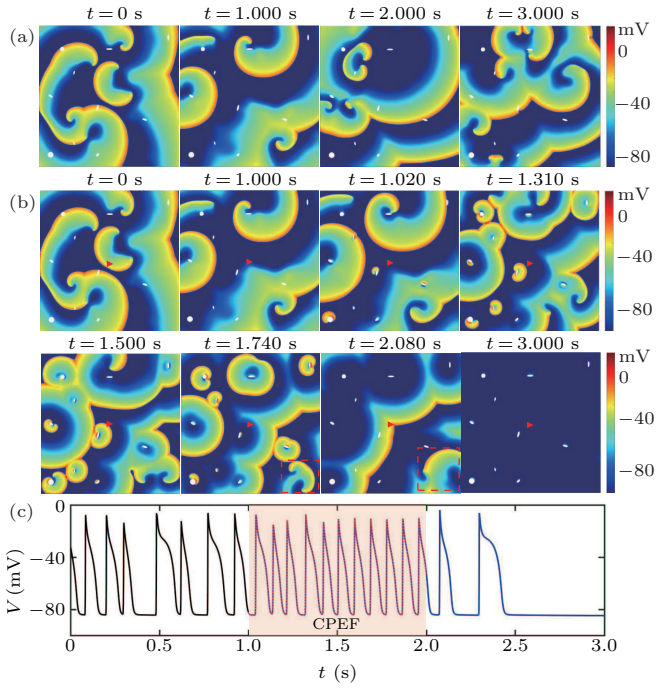


Fig. 7. Suppression of two-dimensional spiral turbulence by CPEF. (a) Spiral turbulence. (b) Applied CPEF from 1 s to 2 s, the electric strength is 0.6 V·cm^{-1}. (c) The membrane potentials of the red location in (b) over times.

As demonstrated in Fig. 7(b), a CPEF with an electric field strength of 0.6 V·cm^{-1} and an angular frequency of 0.14 rad·ms^{-1} was initiated at $t = 1.00$ s, and this was maintained for 1 s. At $t = 1.02$ s, excitation waves began to emerge around specific defects and propagate outward. However, throughout the process, the subset of defects capable of generating excitation waves exhibited periodic fluctuations, with their number also demonstrating variability. This phenomenon can be attributed to the dynamic properties of the excitable medium, wherein re-excitation necessitates the restoration of the medium to an excitable state in proximity to the resting membrane potential. In certain instances, despite the initiation of waves, the formation of stable circular waves is impeded due to collisions with adjacent turbulent activity. In other cases, defects have not yet fully recovered to an excitable state, rendering wave generation impossible. Nevertheless, under appropriate conditions, each defect retains the capacity to emit excitation waves. At times $t = 1.31$ s and $t = 1.5$ s, the formation of relatively complete circular waves around multiple defects was observed, which then propagated outward. By $t = 1.74$ s, only a few turbulent waves remained in the medium, located within the red dashed box in the lower right corner. At a time of two seconds, the CPEF ceases, thus halting the emission of waves in the vicinity of defects. At $t = 2.08$ s, only two waves remain in the medium. Through repeated interactions and propagation, all wave activity either annihilates or is expelled from the medium. In conclusion, the overall structure reverts to a state of rest.

The analysis indicates that the application of a CPEF can effectively suppress spiral wave turbulence in the presence of multiple defects. Due to the phase-locking phenomenon, the frequency of CPEF was 0.14 rad·ms^{-1}. This resulted in the emission of circular waves from the defects at a frequency of 0.069 rad·ms^{-1}, slightly higher than the initial turbulent frequency of 0.060 rad·ms^{-1}. Notably, successful elimination of spiral wave turbulence is accomplished with an exceptionally low electric field strength of merely 0.6 V·cm^{-1}. This approach is in stark contrast to the clinically established method for eliminating heart vortices, which relies on a high-energy electric shock that depolarizes and hyperpolarizes heart tissue through a voltage gradient of approximately 5 V·cm^{-1}, with external application reaching up to 360 J. CPEF signifies a low-voltage therapeutic strategy, offering a safer and gentler alternative.

4. Discussion

4.1. Mechanisms of eliminating turbulence under multiple defects

The mechanism and effectiveness of electric fields in eliminating turbulent waves under varying defect conditions are of central concern. In single-defect cases, the driving of turbulent waves is primarily reliant upon the generation of high-frequency excitation waves,[29] in accordance with the principle that high frequencies are capable of driving low frequencies.[41,42] It is evident that the higher the frequency of the excitation wave, the faster the turbulent wave will be driven. However, in the event of a significant number of defects being present in the medium, the situation becomes more complex. Research conducted in 2011 demonstrated that excitation waves surrounding defects have the capacity to synchronize the medium's electrical activity, thereby facilitating the suppression of turbulent waves.[10] Provided that excitation waves are generated in the surrounding area, medium synchronization can be achieved, thereby creating conditions for the elimination of turbulent waves.

The findings of the present study demonstrate that CPEF exhibits significant advantages over UEF in the elimination of turbulent waves through multi-defect synchronized excitation. The excitation of a substantial number of excitation waves from more defects is facilitated, achieving more efficient synchronized excitation effects and providing a more effective approach for eliminating turbulent waves. Moreover, the presence of numerous natural defects, such as blood vessels, in real heart tissue renders the discussion of multi-defect scenarios more practically relevant. In scenarios involving multiple defects, numerical simulations demonstrate that when the excitation wave frequency exceeds the turbulent state frequency,

excitation waves are continuously and stably generated around defects. However, the duration of electric field application is not significantly affected by the excitation wave frequency due to the complex interaction between multi-defect distributions and turbulent waves.

Defects in actual heart tissue are frequently complicated and irregular in shape. In computer simulations, random circular and elliptical defects overlap to form more complex defect configurations. As illustrated in Fig. 5, the membrane potential is distributed around circular and elliptical defects in the presence of an external electric field. It has been demonstrated that, in the presence of an external electric field of sufficient intensity, the capacity for membrane potential redistribution at non-uniform boundaries, and the ability to exceed the excitation threshold, is contingent upon the curvature at the respective location. It is evident that, due to its rotational properties, CPEF is capable of consistently locating suitable curvature to generate excitation waves when encountering complex-shaped defects. Consequently, it can be deduced that the intricate geometry of defects exerts a few influences on the excitation waves generated in their surrounding areas. However, under the influence of complex turbulent waves, the collision between excitation waves generated by complex defect shapes and turbulent waves can lead to more complex dynamic behaviour, warranting further investigation and discussion.

4.2. The success rate of driving turbulence

In order to further investigate the influence of electric fields on turbulent waves, a number of defect configurations for different turbulent waves were randomly generated and the CPEF was applied. An in-depth analysis was then conducted to ascertain the effect of the duration of electric field application on the expulsion of turbulent waves. Research has demonstrated that, due to the rotational characteristics of the CPEF, the onset time of its virtual electrode is not constrained by turbulent conditions. During the chaotic propagation of turbulent waves, excitation waves are generated around each defect, exerting a driving effect on the turbulent waves. As an increasing number of defect-induced excitation waves are generated, the medium gradually synchronizes with these excitation waves, causing the turbulent waves to dissipate. Given that the state of the turbulent waves varies at different times in each specific scenario, the duration of the applied electric field is not fixed. However, the criterion for ceasing the application of the electric field remains consistent each time: when nearly all defects within the medium have generated excitation waves and the medium begins to synchronize with these excitation waves, the electric field is discontinued. At this juncture, the medium reverts to its quiescent state. Furthermore, in the present study, CPEF is applied continuously. However, given the established lock-in relationship between the applied electric field and the frequency of the excitation waves generated, further consideration will be given to the implementation of a pulsed electric field in subsequent studies. It is important to note that each pulse corresponds to one CPEF rotation cycle, with the objective of minimizing energy loss. In our 2022 publication,[34] we presented data on the success rate for single-defect-driven turbulent waves. The application of the electric field was extended for a duration of 2 s, resulting in a substantial increase in the success rate from 15% to 100%. However, in the current numerical simulation process, when confronted with more complex defect configurations, the success rate of driving turbulent waves exhibits significant variation for each distinct defect arrangement and turbulent waves. The duration of electric field application continues to exert a substantial influence on this success rate. It is evident that considering only a single multi-defect scenario is inadequate in terms of both representativeness and generalizability. To achieve more comprehensive and reliable results, further numerical simulations are necessary. This will become a key focus of our subsequent research, and we will continue to explore it in depth.

5. Conclusion

The present study establishes the efficacy and mechanism of low-energy defibrillation using CPEF, targeting life-threatening ventricular fibrillation. It has been confirmed that CPEF leverages myocardial heterogeneities as virtual electrodes, thereby generating localized polarization and eliciting excitation waves. In contrast to the fixed directionality of the UEF, the rotating CPEF vector enables precise adaptation to the complex distribution of heart tissue defects. In a myocardial model incorporating multiple defects of varying sizes, shapes, and non-uniform spatial distribution, CPEF at only 0.6 $\mathrm{V{\cdot}cm^{-1}}$ successfully induced excitation waves to terminate arrhythmia. In the context of spiral wave turbulence, periodic excitation from CPEF polarized regions has been shown to progressively suppress chaotic activity and restore electrophysiological stability. This study demonstrates that CPEF offers significant advantages and considerable potential as a low-energy, non-invasive strategy for treating arrhythmia. It is anticipated that, in view of the ongoing enhancement and validation of technology, CPEF has the potential to emerge as a promising low-energy alternative for clinical arrhythmia intervention.

Acknowledgments

Project supported by the National Natural Science Foundation of China (Grant No. 11647055), the Natural Science Basic Research Program of Shaanxi Province (Grant Nos. 2024JC-YBMS-073, 2024JC-YBMS-074, and 2023-JCQN-0013), the Scientific Research Program Funded by Shaanxi Provincial Education Department (Grant

No. 23JK0604), and the National College Students Innovation and Entrepreneurship Training Program of Xi'an Shiyou University (Grant No. 202310705020).

References

[1] Liu M B, He X Y, Yang X H and Wang Z W 2025 *Chin. Gen. Pract.* **28** 20
[2] Weiss J N, Qu Z L, Chen P S, Lin S F, Karagueuaian H S, Hayashi H, Garfinkel A and Karma A 2005 *Circulation* **112** 1232
[3] Karma A 2013 *Annu. Rev. Condens. Matter. Phys.* **4** 313
[4] Qu Z, Hu G, Garfinkel A and Weiss J N 2014 *Phys. Rep.* **543** 61
[5] Buchan S, Kar R, John M, Post A and Razavi M 2023 *Cardiovas. Drug. Ther.* **37** 323
[6] Fast V G, Rohr S, Gillis A M and Kleber A G 1998 *Circ. Res.* **82** 375
[7] Woods M C, Sidorov V Y, Holcomb M R, Beaudoin D L, Roth B J and Wikswo J P 2006 *Heart Rhythm* **3** 751
[8] Pumir A and Krinsky V 1999 *J. Theor. Biol.* **199** 311
[9] Pumir A, Nikolski V, Hörning M, Isomura A, Agladze K, Yoshikawa K, Gilmour R, Bodenschatz E and Krinsky V 2007 *Phys. Rev. Lett.* **99** 208101
[10] Luther S, Fenton F H, Kornreich B G, Squires A, Bittihn P, Hörnung D, Zabel M, Flanders J, Gladuli A, Campoy L, Cherry E M, Luther G, Hasenfuss G, Krinsky V I, Pumir A, Gilmour R F and Bodenschatz E 2011 *Nature* **475** 235
[11] Shajahan T K, Berg S, Luther S, Krinski and Bittihn P 2016 *New J. Phys.* **18** 043012
[12] Ji Y C, Uzelac T, Otani N, Luther S, Gilmour R F, Cherry E M and Fenton F H 2017 *Heart Rhythm* **14** 1254
[13] Mahanta D and Dutta S 2018 *Phys. Rev. E* **98** 052206
[14] Mulimani M K, Alageshan J K and Pandit R 2020 *Phys. Rev. Research* **2** 023155
[15] Chen J X, Zhang H and Li Y Q 2006 *J. Chem. Phys.* **124** 014505
[16] Schmidt S and Ortoleva P 1977 *Phys. Rev. Lett.* **76** 3854
[17] Steinbock O, Schütze J and Müller S 1992 *Phys. Rev. Lett.* **68** 248
[18] Krinsky V, Hamm E and Voignier V 1996 *Phys. Rev. Lett.* **76** 3854
[19] Ji L, Zhou Y, Li Q, Qiao C and Ouyang Q 2013 *Phys. Rev. E* **88** 042919
[20] Li T C, Gao X, Zheng F F, Pan D B, Zheng B and Zhang H 2017 *Sci. Rep.* **7** 8657
[21] Xia Y X, Zhi X P, Li T C, Pan J T, Panfilov A V and Zhang H 2022 *Phys. Rev. E* **106** 024405
[22] Gray R A, Pertsov A M and Jalife J 1998 *Nature* **392** 75
[23] Witkowski F X, Leon L J, Penkoske P A, Giles W R, Spano M L, Ditto W L and Winfree AT 1998 *Nature* **392** 78
[24] Feng X, Gao X, Pan D B, Li B W and Zhang H 2014 *Sci. Rep.* **4** 4831
[25] Pan D B, Gao X, Feng X, Pan J T and Zhang H 2016 *Sci. Rep.* **6** 21876
[26] Punacha S and Shajahan T K 2020 *Phys. Rev. E* **102** 032411
[27] Li T C, Ai B Q, Chen Y and Li B W 2021 *Phys. Lett. A* **388** 127058
[28] Hu Y, Ding Q, Wu Y and Jia Y 2023 *Chaos Solitons Fractals* **175** 113957
[29] Feng X, Gao X, Tang J M, Pan J T and Zhang H 2015 *Sci. Rep.* **5** 13349
[30] Feng X and Gao X 2019 *Nonlinear Dyn.* **98** 1919
[31] O'Connor C E, Brady E, Zheng Y, Moore E and Stevens K 2022 *Nat. Rev. Mater.* **7** 702
[32] Luo C H and Rudy Y 1991 *Circ. Res.* **68** 1501
[33] Qu Z L, Kil J, Xie F G, Garfinkel A and Weiss J N 2000 *Biophys. J.* **78** 2761
[34] Feng X, Yin X L, Wen J Q, Wu H and Gao X 2022 *Chaos* **32** 093145
[35] Fenton F H, Cherry E M, Karm A and Rappel W J 2005 *Chaos* **15** 013502
[36] Vignal P, Collier N, Dalcin L, Brown D L and Calo V M 2017 *Comput. Methods Appl. Mech. Engrg.* **316** 1179
[37] Weidmann S 1951 *J. Physiol.-London* **115** 227
[38] Agladze K, Kay M W, Krinsky V and Sarvazyan N 2007 *Am. J. Physiol. Heart Circ. Physiol.* **293** H503
[39] Petrov V, Ouyang Q and Swinney H L 1997 *Nature* **388** 655
[40] Lin A L, Bertram M, Martinez K and Swinney H L 2000 *Phys. Rev. Lett.* **84** 4240
[41] Hendrey M, Ott E and Antonsen T M Jr 2000 *Phys. Rev. E* **61** 4943
[42] Luo J M, Zhang B S and Zhan M 2009 *Chaos* **19** 033133